Available online at www.sciencedirect.com
ScienceDirect
Journal of Magnetic Resonance 183 (2006) 167–177
JMR Journal of Magnetic Resonance
www.elsevier.com/locate/jmr

# Low magnetic fields for flow propagators in permeable rocks

Philip M. Singer *, Gabriela Leu, Edmund J. Fordham [1], Pabitra N. Sen

*Schlumberger-Doll Research, 36 Old Quarry Road, Ridgefield, CT 06877, USA*

Received 7 June 2006; revised 16 August 2006
Available online 7 September 2006

**Abstract**

Pulsed field gradient NMR flow propagators for water flow in Bentheimer sandstone are measured at low fields ($^1$H resonance 2 MHz), using both unipolar and bipolar variants of the pulsed gradient method. We compare with propagators measured at high fields ($^1$H resonance 85 MHz). We show that (i) measured flow propagators appear to be equivalent, in this rock, and (ii) the lower signal to noise ratio at low fields is not a serious limitation. By comparing different pulse sequences, we study the effects of the internal gradients on the propagator measurement at 2 MHz, which for certain rocks may persist even at low fields.


*Keywords:* Low magnetic fields; Flow propagators; Internal gradients; Signal to noise ratio

## 1. Introduction

Increasingly, laboratory nuclear magnetic resonance (NMR) measurements are being made at ever-higher magnetic fields to enhance resolution and signal to noise ratio ($S/N$ or SNR). In a different context, NMR at low magnetic fields ($^1$H resonance frequency $\omega_0/2\pi \lesssim 2$ MHz), and with low-resolution magnets, is now widely used as a borehole measurement in petroleum and other geophysical exploration [1,2]. With the growing demand for hydrocarbons there is an immense and imminent need for developing new NMR laboratory techniques, for application to sedimentary rocks and other porous media, at these lower frequencies.

A laboratory technique receiving much current attention is the measurement of the NMR flow propagator [3–15] and the NMR time-of-flight technique [16–18]. This is mainly because the largest length scales that can be probed by diffusion and relaxation measurements [19–21] are ~100 μm, which can be less than the size of the largest pores in some rocks, especially carbonates (limestones and dolomites). Furthermore the actual physics of flow in complex porous media is of interest in a wide range of processes in chemical, geological, and biological systems. Dispersion, the transport of molecules or tracers due to combined effects of diffusion and fluid flow at low Reynolds number, is an important problem both in the fundamentals of hydrodynamics [22–24] and in its application in diverse fields including biological perfusion, chemical reactors, soil remediation and oil recovery. These flow processes are controlled by the nature of the interconnections, and the topology of the pore space over length scales equivalent to many pores. Although for highly heterogenous samples, multiple length scales can be important [7,8,12,24–27] and not all are accessible by NMR methods, the NMR flow propagators can nevertheless probe displacements of the order of ~5 mm. This is almost two orders of magnitude larger than those achievable by the diffusion and relaxation methods currently used, in petroleum industry practice, as probes of the rock pore space.

Hitherto, most laboratory pulsed-field-gradient (PFG-NMR) experiments measuring flow propagators and dispersion in porous media have used high (typically 85 MHz $^1$H resonance) magnetic fields [3–9,11–16,18]. The advantage of high fields in SNR is well-known; their draw-back is a strong increase in the deleterious effects of

* Corresponding author.
*E-mail address:* psinger@slb.com (P.M. Singer).
[1] Present address: Schlumberger Cambridge Research, Cambridge, CB3 0EL, UK.

1090-7807/$ - see front matter © 2006 Elsevier Inc. All rights reserved.
doi:10.1016/j.jmr.2006.08.006

induced internal field gradients. Contrast in magnetic susceptibility $\Delta\chi$ between fluid components and solids gives rise to induced internal field gradients $g_{\text{int}}$ which increase with static field $B_0(=\omega_0/\gamma)$. These may be reduced by reductions in $B_0$. The reduction is at least linear; in [28] it is shown that diffusion in the larger pores imposes a maximum effective gradient $g_{\max}$, which scales super-linearly as $B_0^{3/2}$. For the first time, we compare the propagators measured at low fields (2 MHz present work) to those determined at high fields (85 MHz [14]) using adjacent core-plugs *and* using similar pulse sequences. We conclude that internal gradient effects on the flow propagator can be satisfactorily ameliorated at high fields if (but only if) the correct pulse sequence is used. At low fields, internal gradients are greatly reduced, and more protocol options are available in PFG experiments [29]. In particular, we show that the unipolar PFG archetypes [30,31] are usable when internal gradients are sufficiently small. Even when they persist, as in our study rock, the unipolar protocols remain marginally acceptable, subject to a small penalty on SNR and larger systematic errors on the moments of the propagator.

Flow propagators may also be measured at low fields with fixed-field-gradients (FFG) in the fringing field of a superconducting magnet [32]. However, unlike the PFG experiments used here, only a more limited number of FFG pulse sequences can be used in fringe fields. In particular there are no analogues of the bipolar variants available in PFG experiments. Our data implies that in the case of our study rock (a sandstone), FFG experiments would be subject to quantitative errors in the propagator measurement even at low fields, whilst in many carbonates they would not.

We consider the signal to noise ratio SNR of the low field experiments in more detail. According to [33] this scales as $\omega_0^{7/4}$ for equivalent resonator geometries. A mitigating factor is the solenoid resonator geometry used in our low-field system. This yields an advantage (relative to a saddle coil) of a factor ~3.1 [33] additional to the frequency scaling. At 2 MHz, relative to 85 MHz, we estimate a reduction in SNR of ≃245 (see Appendix C). Nevertheless, our practical results show that this is not a serious limitation, and dispel previous misconceptions about SNR limitations for flow propagator measurements at low fields.

## 2. Experimental

PFG-NMR propagator experiments measure the statistical distribution of fluid displacements ($\zeta$) for a chosen mean flow velocity ($v$) during a chosen flow evolution time ($\Delta$). The (tunable) length scale in PFG-NMR experiments is given by $\langle\zeta\rangle_0 = v\Delta$, where $\langle\zeta\rangle_0$ is the mean displacement during time $\Delta$ along the mean flow direction ($\hat{y}$), i.e. $\langle\mathbf{v}\rangle = [0, v, 0]$. $v$ is a volume-average "interstitial" or capillary flow velocity given by $v = \dot{V}/A\phi$, where $\dot{V}$ is the imposed volumetric flow rate, and $A$ and $\phi$ are the cross-sectional area and porosity of the rock, respectively. For the flow rates $\dot{V}$ used here, the maximum capillary flow velocity was $v = 1.10\ \text{mm s}^{-1}$. From the measured permeability (~2 μm$^2$), one can estimate a mean capillary diameter $d \sim 30\ \mu\text{m}$ [34], implying a low Reynolds number $Re \simeq 0.03$ and a large Péclet number $Pe \simeq 15$ regime.

By incrementing values of $q = \gamma\delta g_y$, the magnetization wave vector set up by the pulsed gradients, the entire probability distribution function of these displacements $P(\zeta|\Delta, v)$ may be determined. This is the NMR "Flow Propagator", for chosen $\Delta$ and $v$. Alternatively, a more limited measurement of the moments of the distribution of $P(\zeta|\Delta, v)$ may be attempted. Both approaches have been applied to flow through mono-disperse bead packs and rocks [3–9,11–14,16,18]. Here, we demonstrate the feasibility of both methods at 2 MHz.

### 2.1. Rock, core-holder and NMR system

The flow experiments were performed on Bentheimer sandstone, a German building sandstone. The aeolian origin is reflected in a low proportion of clays, and a high hydraulic (Darcy) permeability. Typically about 2 μm$^2$, this would be regarded as unusually high for a reservoir rock. In Section 4 we also compare the Bentheimer data to Indiana Limestone for the case of no flow.

Porosity as determined by Boyle's Law helium pycnometry was $\phi = 23$ p.u. ("p.u." means "porosity units", where 1 p.u. ≡ 1%). The rock was saturated in a NaCl brine of conductivity $5\ \text{S m}^{-1}$. Porosity measured with NMR using a CPMG sequence [35], was $\phi = 22.2$ p.u. The small discrepancy in measures of porosity is common, and can be due to several reasons such as imperfect saturation of the rock (residual air), surface or corner flaws causing shape deviations from a right cylinder, and volume changes by swelling of water-sensitive clays. Because of a degraded SNR, the original brine was replaced by deionized water; the NMR porosity was further reduced to $\phi = 21.5$ p.u. Clay swelling under reduced salinity is a plausible explanation. During the multiple months of flowing deionized water and NMR data acquisition, the porosity $\phi =$ 21.5 p.u. was stable within ±0.2 p.u.

The rock was a cylinder of diameter 1.5 in. nominal (≃38 mm) and length 62 mm. The diameter 1.5 in. is a standard size in petrophysics laboratory where accurate porosity measurements are critical; measurement accuracy (for any method) rapidly deteriorates in practice for smaller diameter cores. This necessitates both a core holder, and a magnet, probe and gradient system based on such physical sample sizes. The NMR system [Oxford Instruments, Abingdon, UK; model "Big-2"] with "Maran-DRX" console] consists of a 50 mT (nominal) permanent magnet thermostated to 30 °C, equipped with a 53 mm solenoid resonator and "slab" format field gradient coils.

A custom-made core holder [ErgoTech Ltd, Conwy, UK] (Fig. 1), was used for mounting the rock sample. A glass-fibre/PEEK (poly(ether-ether-ketone)) composite pressure tube confines all pressurized fluids radially, but

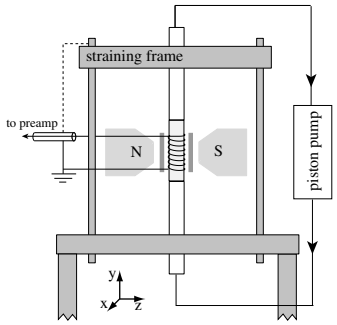


Fig. 1. Schematic of the core-holder and NMR system used. The straining frame is constructed from an austenitic (Grade 316) stainless steel, widely described as "non-magnetic". (Small differences in sample linewidth are detectable but minor.) The "Big-2" magnet assembly (not shown) fits within the steel frame with the NMR coil around the composite pressure tube. Also shown is the flow loop to the piston pump, and its grounding to the NMR system *via* the steel frame (dotted line).

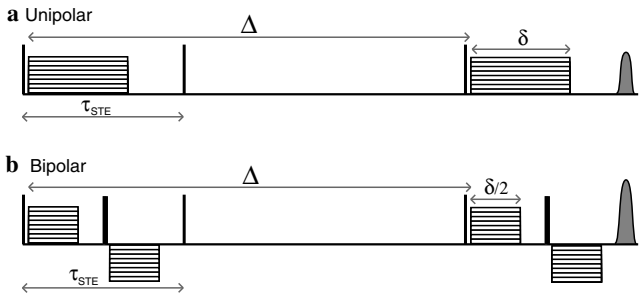


Fig. 2. (a) Tanner's unipolar PFG sequence [30], and (b) Cotts' "13-interval, Condition I" bipolar gradient sequence [36]. Thin (thick) vertical lines indicate 90° (180°) r.f. pulses (of duration $t_{90} = 21$ μs), layered boxes indicate incremented gradient pulses $|g_y| \leqslant 25$ G cm$^{-1}$ (cycle through opposite polarity not illustrated) of duration $\delta = 4$ ms, $\tau_{\mathrm{STE}} = 8$ ms is the encoding time, and the grey bump indicates the stimulated echo (STE). $\Delta$ is the tunable flow evolution or measurement time [8,10], where $\Delta \leqslant 2$ s.

does not carry any axial stress. A novel feature of the design is that axial loads are taken on the external straining frame. A per-fluorinated oil [3M™ Inc., USA; Fluorinert™ grade FC-40] is used to confine the rock under pressure in a rubber sleeve. The system operates at isotropic pressures to ~24 MPa (240 bar ≃ 3500 psi), and by heating and circulating the confining fluid, temperatures to 120 °C may be used. As shown in Fig. 1, it is also equipped with an external fluid pathway to and from the rock used for the water flow. Also shown on the schematic is a grounding path from the core-holder's strain frame to the spectrometer's common ground. As detailed in Appendix C, the additional noise which arises when flowing conductive saline solution instead of deionized water can be reduced by grounding the conductive flow line (which is in contact with the straining frame) to the spectrometer.

A homogeneous fluid saturation was confirmed using NMR profiles (1-D images). De-ionized water at 25 °C was pumped through the rock with a dual-cylinder piston pump [Teledyne-ISCO, USA; model 1000D] at a mean flowrate of $\dot{V} = 16.2$ mL min$^{-1}$. A continuous pressure drop $\Delta p \simeq 90$ kPa (13 psi) was raised across the rock at this flowrate.

### 2.2. Pulse sequences

In Fig. 2 we show typical PFG-NMR pulse sequences used for measuring the flow propagator [8,29,30,36–38]. The initial set of gradient pulses are used to encode the positions $y(0)$ of the fluid's polarized nuclei at an initial time $t_0$, while the second set are used to decode the fluid displacement $\zeta = y(\Delta) - y(0)$ at a later time $t_0 + \Delta$. The observed PFG-NMR signal takes the form a stimulated echo (STE), whose intensity is given by the ensemble average over all polarized spins $S(q) = \langle e^{iq\zeta} \rangle$, where: $q = \gamma \delta g_y$ is the magnetization wavenumber, $\gamma/2\pi = 4257$ Hz G$^{-1}$ is the gyro-magnetic ratio of protons, $g_y$ is the amplitude of the PFG along the flow direction ($\hat{y}$), and $\delta$ is the gradient duration time. The signal $\langle e^{iq\zeta} \rangle = \int P(\zeta'|\Delta, v) e^{iq\zeta'} d\zeta'$ is measured for a set of 128 values of $q$ between $\pm q_{\max}$. Optimized choice and interpolation of the $q$ values are as described in [14]. More generally, the magnetization "grating" $e^{iq\zeta}$ should be written $e^{i\mathbf{q}\cdot\boldsymbol{\zeta}}$ for general wavevectors $\mathbf{q}$ and vector displacements $\boldsymbol{\zeta}$ but in this paper only unidirectional field gradients selecting displacement components $\zeta$ in the $y$ direction are considered. Propagators $P(\zeta|\Delta, v)$ are then determined by inverse Fourier transform of the data set. Typical examples of NMR propagator are shown in Fig. 3, the details of which are discussed in Section 5.

Two different pulse sequences are used in this study. The original Tanner [30,31] sequence, shown in Fig. 2(a), uses unipolar gradient pulses, whilst the Cotts 13-interval sequence [36], shown in Fig. 2(b), uses bipolar gradient pulses with 180° r.f. refocussing pulses interposed between the opposed-polarity gradient pulses (see Appendix B). The

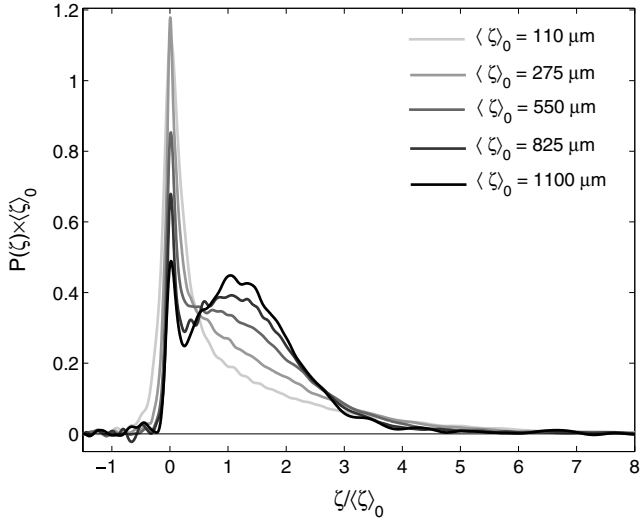


Fig. 3. Probability distribution function $P(\zeta|\Delta, v)$ of fluid displacements $\zeta$ using the bipolar sequence for various flow evolution times $\Delta = \{0.1, 0.25, 0.5, 0.75, 1\}$ s. The axes are scaled by the nominal mean displacement $\langle\zeta\rangle_0 = v\Delta$, and a fixed flow rate of $v = 1.10$ mm s$^{-1}$ was used.

bipolar pulse sequence reduces the effects of induced internal gradients typical for porous media. In the high field (85 MHz) case, the bipolar pulse sequence is used universally. In the low field case, where internal gradients are expected to be lower by at least a factor of 40, the unipolar sequence may be feasible for some rocks. In the next section we compare low and high field propagators using the bipolar sequence, while in Section 4 we compare the bipolar and unipolar sequences, and the effect of the remaining internal gradients at 2 MHz.

## 3. High vs. low-field propagators

In Fig. 4 we compare the flow propagators for similar (adjacent cores, cut from the same block) Bentheimer sandstone rocks under similar experimental conditions. The 2 MHz (present study) is taken with $\Delta = 0.45$ s and $v = 1.10$ mm s$^{-1}$, while 85 MHz [14] used $\Delta = 0.45$ s and $v = 1.03$ mm s$^{-1}$. We conclude that measurements at 2 MHz present no difficulty, and that the propagators are very similar at low (2 MHz) and high (85 MHz) fields. The small differences shown in Fig. 4 could be due to (a) salinity effects on the rock, (b) the fact that the cores are not identical, and/or, (c) different internal gradient artifacts.

Different salinities used could partly explain the differences in Fig. 4. For 2 MHz (present study) we flowed deionized water across the rock in order to reduce the noise in our experiment (see Appendix C), whereas the high field data taken from [14] used brine. However, it is known that low salinity water (especially deionized water) tends to cause swelling of any clays in the rock, which may reduce the porosity. As mentioned earlier, the NMR measured porosity for deionized water saturation ($\phi = 21.5$ p.u.) was slightly lower than for brine saturation ($\phi = 22.2$ p.u.), which could account for the small differences in pore geometries. It is also possible that the differences are due to the cores not being identical, however, we note that the coreplugs were drilled from adjacent parallel positions in the same core.

Finally, it is possible that the internal gradient artifacts on the propagators are not identical between low and high field. As mentioned in Section 2, the bipolar sequence is designed to minimize such internal field effects, however, the bipolar sequence can only eliminate uniform (i.e. constant) internal gradients. If, on the other hand, the internal gradients vary significantly during the encoding time $\tau_{STE}$, no pulse sequence exists which can properly refocus such a fluid trajectory, especially at high fields (although further improvements can be implemented [39]).

We conclude from Fig. 4 that the differences between high and low field data are not large, for this rock (quantitative differences and their origins are beyond the scope of this paper). Since the internal gradient heterogeneities must scale linearly with $B_0$ in their point values, and more strongly ($\sim B_0^{3/2}$ [28]) in their effect on diffusion (a factor $\sim$280 for our two fields), the agreement of Fig. 4 implies that internal gradient heterogeneities over pore length scales are not a serious interference with the propagator measurement in this rock, at either field, provided that the bipolar sequence is used. This may not be the case for other sandstones where susceptibility contrasts can be very much larger. As exemplified in Fig. 5, internal gradients may become negligible for carbonate rocks at 2 MHz (in the static situation), and the unipolar archetype sequence is then usable without artifact. This is never the case at 85 MHz where use of the bipolar sequence, with real sedimentary rocks of any type, is universal.

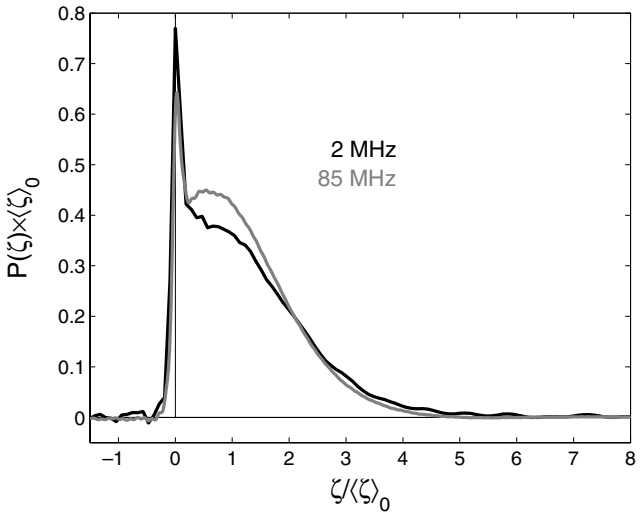


Fig. 4. High vs. low-field flow propagator for similar Bentheimer rocks (adjacent cores, cut from the same block) and similar experimental conditions, both using the bipolar sequence. Data at 2 MHz (present study) used $\Delta = 0.45$ s and $v = 1.10$ mm s$^{-1}$, while data at 85 MHz (taken from Scheven et al. [14]) used $\Delta = 0.45$ s and $v = 1.03$ mm s$^{-1}$.

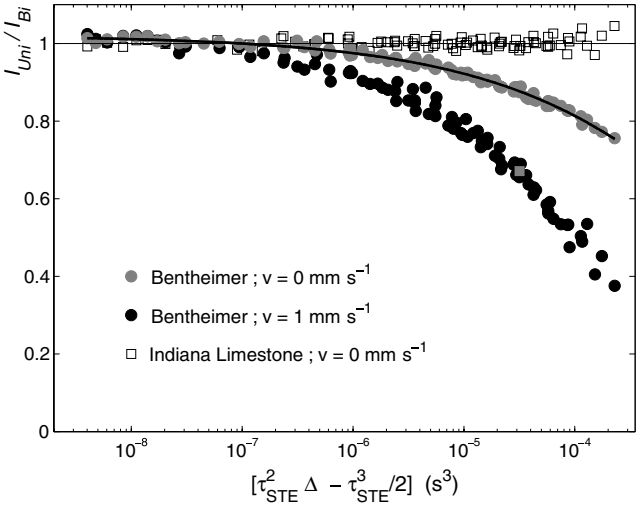


Fig. 5. Ratio of unipolar to bipolar STE signal intensity ($I_{Uni}/I_{Bi}$) as a function of $\tau_{STE}^2\Delta - \tau_{STE}^3/2$ (in s$^3$) for a fixed set of values 1 ms $\leqslant \tau_{STE} \leqslant$ 15 ms and 4 ms $\leqslant \Delta \leqslant$ 1 s, and zero applied gradients (i.e. $g_y = 0$). In the case of the Bentheimer, the signal decay is entirely due to internal gradients $g_{int}$ at 2 MHz; the effect is enhanced with flow. Black curve shows fit detailed in Appendix A. In the case of Indiana Limestone, no observable effect in this range is found for the stationary case.

## 4. Unipolar vs. bipolar sequences at 2 MHz

Interpretation of the flow propagator generally assumes that there are no internal field gradient effects. The presence of internal gradients distorts the propagator and quantitative accuracy is degraded. As discussed in Section 3, the bipolar PFG sequence reduces but does not eliminate these internal gradient effects. In FFG experiments however (as in fringe fields or in a bore-hole tool), there is no analogue of the bipolar sequence. In this section, we discuss distortions of the propagator under the unipolar sequence, in the presence of internal gradients, which are found to persist even at 2 MHz for certain rocks.

Surface relaxation processes, and susceptibility induced variations of the internal fields (produced by the susceptibility mismatch between fluid and matrix) affect nearly all flow NMR measurements through porous media, even at 2 MHz. As shown in Fig. 5, we found that the use of the unipolar pulse sequence (or "7-interval" [36] sequence) gave a reduced STE intensity $I_{\mathrm{Uni}}$ as compared to the bipolar pulse sequence STE intensity $I_{\mathrm{Bi}}$. This is a result of the effect of internal field gradients $g_{\mathrm{int}}$ in the unipolar sequence, which are (partially) cancelled in the bipolar sequence.

For comparison, we show also $v = 0$ data for a contrasting rock, Indiana Limestone, an outcrop limestone of significant internal geometric heterogeneity but low contrast in magnetic susceptibility. In this case there is no observable difference between $I_{\mathrm{Uni}}$ and $I_{\mathrm{Bi}}$ for all values of $\tau_{\mathrm{STE}}^2\Delta - \tau_{\mathrm{STE}}^3/2$, demonstrating that internal gradients are negligible in this rock, at least for the stationary case. This was previously shown for diffusion data, in [29]. The contrast in behavior between sandstones and carbonates is supported by the susceptibility data in [28], where the distributions of susceptibility contrast $\Delta\chi$ in over 320 sandstones and carbonates show median $\Delta\chi$ values at least one order of magnitude different between the two rock classes. It is also in accord with common empirical experience in many other NMR experiments on rocks. Whether the bipolar sequence is required at 2 MHz will depend on the magnitude of the internal fields. From the data of [28], and the specific cases in Fig. 5 and [29], we conjecture that the bipolar sequence will be preferred in the majority of sandstones, but unnecessary in many carbonates.

The data for Bentheimer can be understood qualitatively as follows. Using Cotts' formulation, the intensity ratio for $g_y = 0$ is approximately given by [36]

$$\frac{I_{\mathrm{Uni}}}{I_{\mathrm{Bi}}} \simeq \exp\left(-\gamma^2 g_{\mathrm{int}}^2 D_0 \cdot \left[\tau_{\mathrm{STE}}^2\Delta - \tau_{\mathrm{STE}}^3/2\right]\right) \quad (1)$$

Strictly speaking, Eq. (1) applies only for free diffusion (without flow) in a uniform background gradient, and is thus an approximate description of the data for flow in rocks. Nevertheless, the decay in the data set is evident, and the decay collapses well to $\tau_{\mathrm{STE}}^2\Delta - \tau_{\mathrm{STE}}^3/2$ over a wide range of $1\,\mathrm{ms} \leqslant \tau_{\mathrm{STE}} \leqslant 15\,\mathrm{ms}$ and $4\,\mathrm{ms} \leqslant \Delta \leqslant 1\,\mathrm{s}$ (Fig. 5). This is the analogue to CPMG decays in rocks [28] where scaling by $t_{\mathrm{E}}^2(2n\tau)$ was shown. In the case of the Bentheimer $v = 0$ data, we fit the data to Eq. (1) (black curve in Fig. 5) and estimate the mean internal gradient $g_{\mathrm{irms}} \simeq 0.061\ \mathrm{G\,cm^{-1}}$ (where "irms" = inverse root mean square) for Bentheimer at 2 MHz (see Appendix B for details). We further conjecture that the scaling of Eq. (1) applies in the flowing case also. This is supported empirically by the data in Fig. 5. The decay in $I_{\mathrm{Uni}}/I_{\mathrm{Bi}}$ is more severe when flowing, as molecules move significantly longer distances (and through more fluctuations in the internal field) over the motion-encoding period $\Delta$. This shows that where bipolar sequences are required, even at 2 MHz, for diffusion (non-flowing) measurements, they will be required, *a fortiori*, for Flow Propagator measurements. The conjectured scaling for the flowing case requires further analysis, but substitution of diffusion coefficient by a dispersion coefficient is an obvious ingredient. These developments will be reported elsewhere, as well as the flowing data for Indiana Limestone.

In Fig. 6 we compare the full propagators for the unipolar vs. bipolar sequences, on the same rock. Part (a) shows the observed signal intensity, while (b) shows collapsed data set for more careful comparison. We find that the propagators in (b) scale well for small displacements $\zeta/\langle\zeta\rangle_0 \lesssim 1$ (where $\langle\zeta\rangle_0 = 550\,\mu\mathrm{m}$), whereas the bipolar sequence shows more weight at larger displacements $\zeta/\langle\zeta\rangle_0 \gtrsim 1$ (see Section 5.1). This can be expressed quantitatively by comparing the observed mean displacement

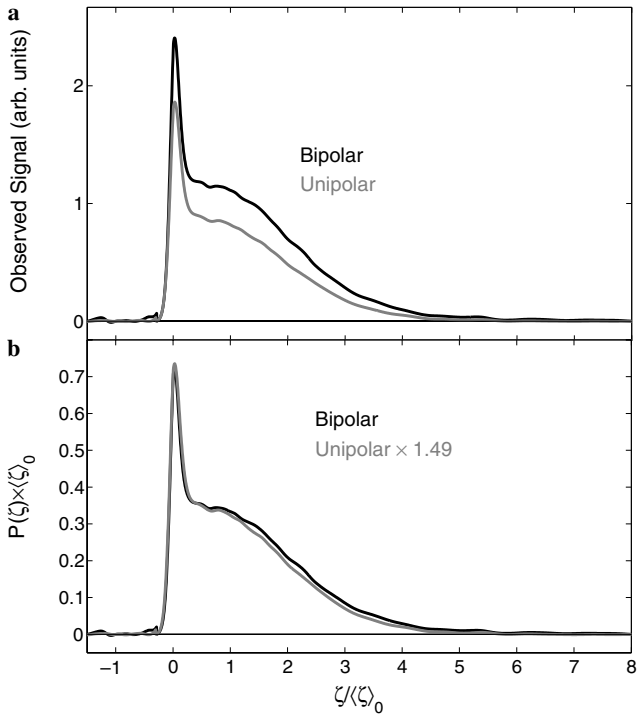


Fig. 6. (a) Unipolar and bipolar propagators for $v = 1.10\ \mathrm{mm\,s^{-1}}$, $\Delta = 500$ ms, and $\tau_{\mathrm{STE}} = 8$ ms on the *same* rock. Note the overall observed reduction in intensity of $I_{\mathrm{Uni}}/I_{\mathrm{Bi}} \simeq 1/1.49$, which corresponds to the (solid grey square) symbol in Fig. 5 at an abscissa of $= 3.174 \times 10^{-5}\ \mathrm{s^3}$. (b) Same data as in (a) except that the unipolar propagator has been multiplied by 1.49 for more careful comparison.

for the unipolar case $\langle\zeta\rangle_{\mathrm{Uni}}/\langle\zeta\rangle_0 = 1.162$ to the bipolar case $\langle\zeta\rangle_{\mathrm{Bi}}/\langle\zeta\rangle_0 = 1.274$. The fact that both means are larger than unity is discussed in more detail in Section 5.1 in terms of surface relaxation effects. The fact that the mean is slightly smaller for the unipolar suggests that fluid parcels that have traversed several pores and different internal field environments are not properly refocused by the unipolar sequence. This effect must be expected to be much worse at high fields, where use of the bipolar sequence has long been recognized as essential.

Bipolar experiments do however have several disadvantages over unipolar sequences. (1) The transverse evolution time $\tau_{\mathrm{STE}}$ is lengthened adversely with the eddy current delays needed (two vs. one). (2) Correcting tip angle errors in r.f. by phase cycling gets progressively more complicated as the number of r.f. events increases. (3) There are no fixed field gradient (e.g. fringing field) analogues to bipolar pulsed gradient experiments. Bipolar sequences are *necessary* when internal gradients are significant; we find few countervailing advantages when internal gradients are negligible.

## 5. Quantitative propagators and moments analysis

The objective of this paper is to demonstrate that propagator measurements are practical at low fields, and not a detailed discussion of these propagators. However, a brief discussion on the moments analysis is made below to show that the data is of high quality. All moments have been calculated using the "low-$q$" moments of $S(q)$ [14].

Propagators for various flow evolution times $\Delta = \{0.1, 0.25, 0.5, 0.75, 1\}$ s, as a function of displacement are presented in Fig. 3. The axes are scaled by the nominal mean displacement $\langle\zeta\rangle_0 = v\Delta$, for a fixed flow rate of $v = 1.10\ \mathrm{mm\ s^{-1}}$. All data shown in Fig. 3 are for deionized water, corresponding to free diffusion lengths $l_D = (2D_0\Delta)^{1/2}$ ranging from 21 μm to 65 μm, where $\Delta$ is the diffusion time (Fig. 2). $l_D$ is of the order or smaller than the throat-size $d \sim 30$ μm ($d$ is also about a third of the grain sizes). For short $\Delta$, the displacements are mostly ballistic and the shape of the probability distribution for early times reflects that of the local velocity distribution [8]. As $\Delta$ is increased, a double peaked distribution develops which distinguishes the bound (or stagnant) fluid from the flowing fluid. As $\Delta$ is increased further, the bound fluid peak decreases by diffusive coupling to flowing paths, and spectral weight is increasingly shifted from $\zeta \sim 0$ to larger displacements.

We find that the three lowest moments of the distribution are useful to quantify the statistical properties of the flow displacement distributions and their evolution [12,14,40]. These moments are (1) the observed mean displacement $\langle\zeta\rangle$, (2) the standard deviation $\sigma$ and (3) the skewness $\gamma$. They are derived from a cumulant analysis of $S(q) = \langle e^{iq\zeta}\rangle$ over a small range of $q$ space near $q = 0$ as such

$$\ln\langle e^{iq\zeta}\rangle = \sum_{j=1}^{\infty} \frac{(iq)^j}{j!} X_j. \tag{2}$$

$X_j$ are the cumulants, which are related to the moments as such: $X_1 = \langle\zeta\rangle$, $X_2 \equiv \sigma^2 = \langle(\zeta - \langle\zeta\rangle)^2\rangle$, $X_3 \equiv \gamma^3 = \langle(\zeta - \langle\zeta\rangle)^3\rangle$, etc.

The first few moments, as a function of time or mean displacement, provide quantitative measures of dispersion that are useful in comparing different samples, different flow regimes and calculation model systems [12,14]. Furthermore, limiting the data acquisition to the small $q$ range required for the cumulant analysis permits the use of short and weak pulsed field gradients. Short pulses limit signal losses during the spatial coding periods, while weak gradient pulses limit the distortions due to eddy currents induced by the pulsed field gradients. As a compromise, we carried out our moment analysis using a fixed pulse duration $\delta = 4$ ms (see Fig. 2). The maximum fitting range in $q$ space, $q_{\max}$, was determined as the $q$ value where $|S(q_{\max})|/S(0) \sim 0.85$, in other words, the $q$ value where the magnitude of the signal intensity $|S(q)|$ decreased to ~85% of its initial amplitude $S(0)$ at $q = 0$. A gradient list was then generated by selecting ~20 evenly spaced values ranging over $\pm g_{y,\max}$, where $\gamma\delta g_{y,\max} = q_{\max}$. The values for $g_{y,\max}$ used for different $\Delta$ are tabulated in Appendix B.

In Fig. 7 we present the standard deviation (a) $\sigma/\langle\zeta\rangle$, and, the skewness (b) $\gamma/\langle\zeta\rangle$ (both scaled by $\langle\zeta\rangle$) vs. $\langle\zeta\rangle$ for a fixed flow rate $v = 1.10\ \mathrm{mm\ s^{-1}}$ and various evolution times $\Delta$. Grey symbols are raw data, black symbols are recalculated according to Eq. (3) [14]. We see that the skewness, or third moment ($\gamma$), decreases as the mean-

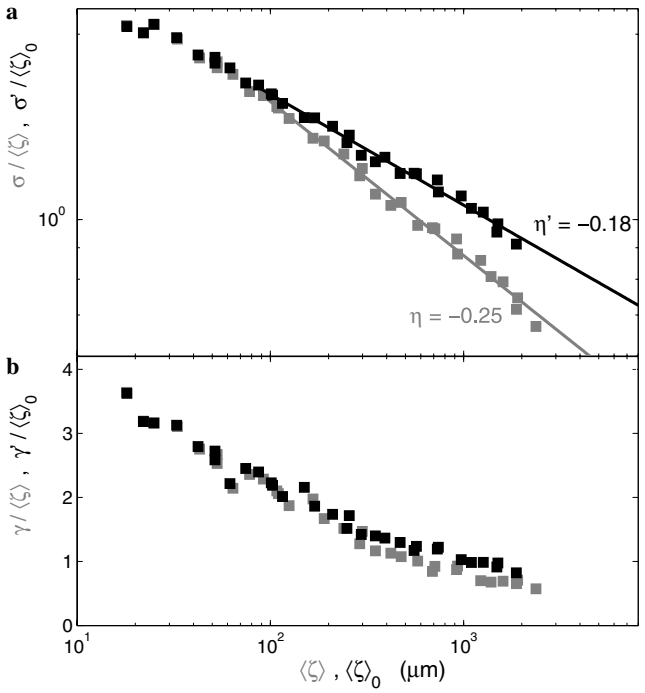


Fig. 7. Observed scaled moments (a) $\sigma/\langle\zeta\rangle$, and (b) $\gamma/\langle\zeta\rangle$ vs. $\langle\zeta\rangle$ (grey symbols) for a fixed flow rate $v = 1.10\ \mathrm{mm\ s^{-1}}$ and various evolution times $\Delta$. Also shown are recalculated values (a) $\sigma'/\langle\zeta\rangle_0$, and (b) $\gamma'/\langle\zeta\rangle_0$ vs. $\langle\zeta\rangle_0$ (black symbols) according to Eq. (3), along with exponent fits in (a). Bipolar sequence used throughout.

displacement increases from 20 to 2000 μm, but does not vanish altogether, indicating that the correlation length for the Lagrangian flow displacement is larger than 2000 μm, i.e. flow is correlated over many grain lengths [8,40].

The approach to Gaussian (where the skewness vanishes) is reflected also in the shape of the propagators Fig. 3. Some spectral weight, which at short times appeared at the largest displacements, has, at later times, shifted toward the mean displacements. When the Taylorian limit is obtained, the displacement distribution is Gaussian, and the distribution of molecular displacements is Gaussian with $\sigma^2 = 2K\Delta$ by definition [22–24], where $K$ is the dispersivity of the sample. For the Taylorian limit one expects $\sigma/\langle\zeta\rangle = \langle\zeta\rangle^{\eta}$ where $\eta \to -0.5$. It is abundantly clear from the second moment analysis that we are in the pre-asymptotic regime.

### 5.1. Relaxation effects

As discussed in Refs. [13,14,39,41], surface relaxation effects can produce undercounting of spins. The presence of such undercounts is signaled by deviations from unity of the ratio of measured mean displacements divided by the nominal mean displacement, $\theta = \langle\zeta\rangle/\langle\zeta\rangle_0$. Deviations of $\theta$ from unity are also observed at 2 MHz as shown in Fig. 8.

For the bipolar case, the ratio rises towards a $\Delta$ independent and approximately steady value of $\theta \simeq 1.29$ for large $\Delta$. It is generally believed that the correlations between surface relaxation and displacement are responsible for removing stagnant (small displacement) spins from the measurement, thereby pushing $\theta$ above unity. In this context it is interesting to note that the time constant for the exponential fit to $\theta$ is ~0.203 s which is within a factor 2 of the log-mean spin-lattice relaxation time $\langle T_1\rangle_{\mathrm{LM}} = 0.390$ s at 2 MHz. A similar, yet slightly smaller effect, was also found at 85 MHz for Bentheimer [14] where $\theta \simeq 1.16$ was found for large $\Delta$ (taking $\phi = 22.2$ p.u. for brine). This frequency difference is possibly a result of increased undercounting of small displacement fluid at lower fields, which is consistent with the fact that surface relaxation is slightly larger at lower frequencies $\langle T_1\rangle_{\mathrm{LM}} \sim \omega_o^{-\alpha}$, where typically $\alpha \lesssim 0.2$ (data of Horsfield in [42]).

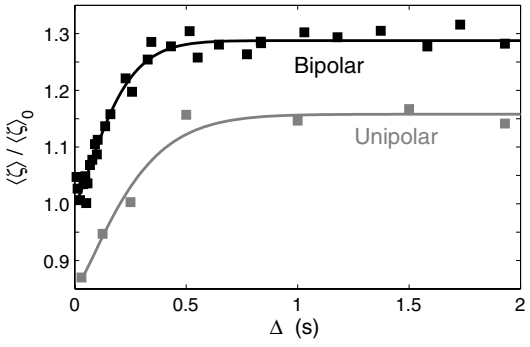


Fig. 8. Deviation of observed from expected mean displacement $\theta = \langle\zeta\rangle/\langle\zeta\rangle_0$ vs. evolution time $\Delta$ for a fixed flow rate $v = 1.10$ mm s$^{-1}$ (porosity is $\phi = 21.5$ p.u.). Lines are exponential fits with $1/e$ times of 0.203(0.256) s for bipolar (unipolar) sequences, respectively.

In Fig. 8 we also show $\theta$ for the unipolar propagator. While the unipolar propagator suffers from the same undercounting of small displacements as the bipolar sequence, it suffers *additional* undercounting from improper refocusing at large displacements (see Fig. 6), thereby decreasing $\theta$ compared to the bipolar sequence. Such undercounting for large displacements is potentially a much greater issue at high fields since internal gradient differences become larger from pore to pore. Indeed, undercounting at large displacements has been observed at high field and short $\Delta$ even for the bipolar sequence [13,41], although sequences have been developed to further reduce such effects [39].

One simple model to take into account undercounting of small displacement fluid was developed in [14]. The authors make some assumptions and construct a perturbed probability distribution $P'$ as such $P' = (1 - \theta^{-1})\delta(\zeta) + \theta^{-1}P(\zeta)$ where $\delta(\zeta)$ is a Dirac function, and successfully recovers the expected mean displacement $\langle\zeta\rangle_0 = \int\zeta P'(\zeta)\,\mathrm{d}\zeta$. In Fig. 7 we show the correctly recalculated moments (a) $\sigma'/\langle\zeta\rangle_0$, and, (b) $\gamma'/\langle\zeta\rangle_0$ plotted against $\langle\zeta\rangle_0$, where $\sigma'$ and $\gamma'$ can be deduced from the old parameters $(\sigma, \gamma, \langle\zeta\rangle, \theta)$ as such [14]

$$\frac{\sigma'^2}{\langle\zeta\rangle_0^2} = \theta\frac{\sigma^2}{\langle\zeta\rangle^2} + (\theta - 1) \tag{3}$$

$$\frac{\gamma'^3}{\langle\zeta\rangle_0^3} = \theta^2\frac{\gamma^3}{\langle\zeta\rangle^3} + 3\theta(\theta - 1)\frac{\sigma^2}{\langle\zeta\rangle^2} + (\theta - 1)(\theta - 2)$$

Eq. (3) is taken from Ref. [14] (and rearranged).

The arbitrary lower limit for the fitting range of $\sigma/\langle\zeta\rangle$ is chosen such that $\langle\zeta\rangle/l_D \geqslant 5$, i.e. the mean dispersive displacements $\langle\zeta\rangle$ are much larger than the mean diffusive displacement $l_D$. We find that the exponent for $\sigma/\langle\zeta\rangle$ tends towards $\eta' \simeq -0.18$ for the recalculated data. This should be compared to that at 85 MHz where $\eta' \simeq -0.22$ [14], i.e. both data indicate a pre-asymptotic regime.

## 6. Conclusions

We have demonstrated the feasibility of low field NMR measurements of fluid displacement distributions (the flow propagator) in Stokes flow in porous media, in the pre-asymptotic dispersion regime. The data quality shows that the well-known loss of SNR at low magnetic fields is not in practice a serious limitation.

The observed similarity between high field (85 MHz, [14]) and low field (2 MHz, present study) flow propagators implies that the bipolar pulse sequence is sufficient in reducing internal gradient artifacts at 85 MHz, for the present rock, although the largest internal gradients at 85 MHz ($g_{\max} \sim 650$ G cm$^{-1}$) are over an order of magnitude larger than the maximum *applied* gradients.

More importantly, the close agreement between results from the unipolar and bipolar sequences at 2 MHz

demonstrates that the effect of internal gradients is much reduced at 2 MHz, and that the unipolar sequence may be feasible in some cases. Comparison of bipolar and unipolar pulse sequences indicates a mean value $g_{\text{irms}} \simeq 0.061\ \text{G cm}^{-1}$ and a maximum $g_{\max} \simeq 2.31\ \text{G cm}^{-1}$ in the study rock; these are now significantly lower than the applied gradients available. In such cases, where internal gradients persist at low fields, the bipolar sequence is preferred for a mild SNR advantage and quantitative accuracy on moments of the propagator; however where susceptibility contrasts are less serious (as is typical for limestones) the bipolar variant may be unnecessary.

We demonstrate that the moments analysis (based on low-$q$ data) previously used at higher fields [14] to extract information about dispersion, is also possible at lower fields.

## Acknowledgments

We gratefully acknowledge Uli M. Scheven for insightful comments and discussions, and Douglas D. Griffin for his technical expertise.

## Appendix A. Effects of asymmetric bipolar pulses

Our implementation of the bipolar sequence Fig. 2(b) is slightly non-ideal in that the gradient pulses are placed asymmetrically with respect to the 180° refocussing pulses [29]. It is shown in [36] that the contribution to the attenuation exponent in $\mathbf{g}_{\text{int}} \cdot \mathbf{g}$ vanishes exactly for the symmetrical disposition. This advantage in interpretation is not available in the chosen timings. However it is also desirable to minimize eddy current effects on the 180° r.f. pulses whilst avoiding unnecessary increases the encoding time $\tau_{\text{STE}}$. We found that eddy currents were sufficiently dissipated $\gtrsim 2$ ms after a gradient pulse was switched off; this duration was coded as an eddy current decay time. Molecular displacements during the encoding and decoding intervals should also be small. For $\tau_{\text{STE}} = 8$ ms a small mean displacement of $v\tau_{\text{STE}} \sim 9\ \mu\text{m}$ is expected; this could be reduced by technical improvements in eddy current compensation but is only increased by a symmetric placing of the gradient pulse pairs.

For the unipolar sequence the leading order cross term in free diffusion is [36]

$$\ln(I_{\text{Uni}}) \simeq \mathrm{O}(g^2) - \gamma^2 D_0 \delta \tau_{\text{STE}} (\mathbf{g} \cdot \mathbf{g}_{\text{int}})(2\Delta + \cdots) + \mathrm{O}\left(g_{\text{int}}^2\right) \tag{A.1}$$

while for the bipolar case the cross term is

$$\ln(I_{\text{Bi}}) \simeq \mathrm{O}(g^2) - \gamma^2 D_0 \delta \tau_{\text{STE}} (\mathbf{g} \cdot \mathbf{g}_{\text{int}}) \tfrac{1}{2}(\delta_1 - \delta_2) + \mathrm{O}\left(g_{\text{int}}^2\right) \tag{A.2}$$

where $\delta_{1,2}$ are the delays before and after the gradient half-pulses. Eq. (A2) vanishes for symmetric timing but, whatever the degree of asymmetry, is clearly always much smaller than for the unipolar case. To our knowledge, no models exist for estimating the magnitude of such "cross terms" in the flowing systems. Precise quantification is difficult in rocks because all cases require a volume integral of $\mathbf{g}_{\text{int}} \cdot \mathbf{g}$, wherein $\mathbf{g}_{\text{int}}$ fluctuates intricately.

Since the cross terms are of $\mathrm{O}(q)$ in the attenuation exponent, their effect on the acquired propagator (a Fourier transform of the $q$-space data) will be to convolve a Lorentzian Point Spread Function (PSF) with the Propagator, of a width not yet estimated *a priori*. However agreement between bipolar and unipolar results at 2 MHz (where the cross terms are very different, by Eqs. (A.1) and (A.2)), and between bipolar results at 2 and 85 MHz (where any term of order $\mathbf{g} \cdot \mathbf{g}_{\text{int}}$ will be worse by a factor of ~40) suggests (albeit not conclusively) that the effective width of the PSF is negligible in all cases, for this rock.

## Appendix B. Estimate of internal gradients

In this Appendix, we discuss the details for estimating the mean value of the internal gradients in Bentheimer using the data in Fig. 5 and the model in Eq. (1). Strictly speaking, Eq. (1) only applies for free diffusion (without flow) in a uniform background gradient. In general the effect of non-uniform internal fields requires a full characterization by the DDIF (decay by diffusion in internal fields) method [43].

Given that there is clearly insufficient long time data in Fig. 5 to do a full inversion [44], we use a stretched exponential variant of Eq. (1) as such

$$\frac{I_{\text{Uni}}}{I_{\text{Bi}}} \simeq I_0 \exp\left(-\left(t^{(3)}/T_e^{(3)}\right)^{\beta}\right) \tag{B.1}$$

where $t^{(3)} = \tau_{\text{STE}}^2 \Delta - \tau_{\text{STE}}^3/2$ is the effective time in units of $\text{s}^3$. The results of the best fit of Eq. (B1) to the data is shown as the black curve in Fig. 5, where $I_0 = 1.029$ is the initial amplitude, $\beta = 0.325$ is the stretch exponent, and the time for the amplitude to drop by $1/e$ is given by $T_e^{(3)} = 0.00858\ \text{s}^3$. We then relate $T_e^{(3)}$ to the mean value $\langle T^{(3)} \rangle$ over the underlying distribution as such [45]

$$\langle T^{(3)} \rangle = \frac{T_e^{(3)}}{\beta} \Gamma\left(\frac{1}{\beta}\right) \tag{B.2}$$

where $\Gamma$ is the gamma function, from which we find $\langle T^{(3)} \rangle = 0.0350\ \text{s}^3$. According to Eq. (1) we can then relate $\langle T^{(3)} \rangle$ to the "irms" (inverse root mean square) value $g_{\text{irms}}$ of the internal gradients as such

$$g_{\text{irms}} \simeq \sqrt{\frac{1}{\gamma^2 D_0 \langle T^{(3)} \rangle}} \simeq 0.061\ \text{G cm}^{-1}. \tag{B.3}$$

To allow for restricted diffusion we make the substitution $D_0 \to D'$ where $D'$ is a restricted diffusion coefficient $D(\Delta)$ [21], i.e. $D(\Delta) \leqslant D_0$ (where $D_0 \simeq 2.13 \times 10^{-9}\ \text{m}^2\ \text{s}^{-1}$ is the free diffusion coefficient for water at 25 °C). Using a

Table A.1
Internal gradient estimates for Bentheimer sandstone, compared to applied gradients

| $^1$H resonance | 2 MHz | 85 MHz |
|---|---|---|
| Intrinsic[a] linewidth $(\Delta\omega/2\pi)$/Hz | 7[b] | 300 |
| Internal gradients (all G cm$^{-1}$) | | |
| Maximum $g_{\max}$ (Eq. (B4)) | 2.31[b] | 650 |
| Average $g_{\text{irms}}$ (Eq. (B3)) | 0.061 | 17[b] |
| Applied gradients (all G cm$^{-1}$) | | |
| $g_{y,\max}$: In low-$q$ data at $\Delta = 15$ ms | 3.01[b] | |
| In low-$q$ data at $\Delta = 1.9$ s | 0.07 | |
| Limit of hardware (nominal) | 25 | |

[a] Linewidths assume a perfectly shimmed magnet.
[b] Indicates extrapolated values assuming $\Delta\omega \propto B_0$, $g_{\max} \propto B_0^{3/2}$ and $g_{\text{irms}} \propto B_0^{3/2}$. Applied gradients $\pm g_{y,\max}$ given for the low-$q$ moments analysis, for extreme values of $\Delta$ (Fig. 7), in addition to the hardware limit.

constant value of $D'$ instead has a negligible effect on our analysis and so $D' \simeq D_0/2$ was used for specificity in Eq. (B3).

We note that $g_{\text{irms}}$ thus deduced is consistent with estimates of the maximum *effective* gradient (in diffusion)

$$g_{\max} \simeq \frac{\Delta\omega^{3/2}}{\gamma D_0^{1/2}} \tag{B.4}$$

[28], where $\Delta\omega$ is the intrinsic linewidth due to the internal gradients. According to the intrinsic linewidth at 85 MHz $\Delta\omega/2\pi \simeq 300$ Hz [14], we deduce that $\Delta\omega/2\pi \simeq 7$ Hz at 2 MHz which according to Eq. (B4) suggests a maximum internal field of $g_{\max} \simeq 2.31$ G cm$^{-1}$ at 2 MHz, and a large-pore to small-pore critical size $l^* \simeq 7$ μm. From both the effective mean value $g_{\text{irms}} \simeq 0.061$ G cm$^{-1}$ and the maximum $g_{\max} \simeq 2.31$ G cm$^{-1}$, we find an internal gradient half spread of $g_{\max}/g_{\text{irms}} \simeq 40$, which is typical in a rock [28].

Our internal gradient estimates are summarized in Table A.1, and compared with the applied pulsed gradients used. The maximum effective gradient $g_{\max}$, at 2 MHz, is an order of magnitude *smaller* than the maximum applied gradients used in our experiments (25 G cm$^{-1}$). At 85 MHz the corresponding $g_{\max} \sim 650$ G cm$^{-1}$ is over 25 times *larger* than the maximum applied gradient. This makes explicit the mandatory use of the bipolar sequence at high magnetic fields and supports our findings that at 2 MHz the effect of internal gradients is typically mild, so the unipolar sequence may be adequate in some cases.

## Appendix C. Noise

There are three main sources of noise: the thermal or Johnson noise in the pick-up coil $N_R$ (including resistive losses plus other losses in the circuit such as dielectric losses in tuning capacitances), noise in the receiver system (typically expressed as the noise factor $F$ of the pre-amplifier) [33], and the noise $N_\sigma$ inductively coupled via our saline flow loop.

### C.1. Thermal noise

The average thermal noise voltage across a coil of resistance $R$ at a given temperature $T_c$ is

$$N_R = (4k_B T_c R\Delta\nu)^{1/2}. \tag{C.1}$$

Here $k_B$ is the Boltzmann constant, $R$ is the (coil) resistance, and $\Delta\nu$ is the band-width. The resistive loss in the coil itself can be large at high frequencies due to skin depth (~45 μm at 2 MHz) effect which leads to $R = (\ell_c/p)(\mu\rho\omega_0/2)^{1/2}$ (~0.5 Ω) for our NMR coil of unwound length $\ell_c$, wire circumference $p$, permeability $\mu$ and resistivity $\rho$ [33]. We then obtain

$$N_R = (a_c \Delta\nu T_c)^{1/2}\omega_0^{1/4} \tag{C.2}$$

where $a_c = 4k_B(\ell_c/p)(\mu\rho/2)^{1/2}$. For a bandwidth of $\Delta\nu = 0.2$ MHz, this predicts $N_R \simeq 5\times10^{-8}$ V. The frequency dependence of the signal $S$ itself goes as $S \simeq \omega_0^2/T_s$, where the first $\omega_0$ comes from Faraday's law of induction, and the other $\omega_0/T_s$ comes from the polarization (where $T_s$ is the sample temperature). Combining relevant terms leads to the following SNR expression [33]

$$\text{SNR} \simeq \frac{\phi V_s n_{sc}^{1/2}}{a g_0 (F\Delta\nu T_c)^{1/2} T_s}\omega_0^{7/4} \tag{C.3}$$

where $\phi V_s$ is the porosity times the rock volume, $a$ is the coil radius, $F = (T_n/T_c + 1)$ is the noise factor of the pre-amplifier with noise temperature $T_n$, $n_{sc}$ is the number of scans acquired (or signal averaging), and $g_0 = 1$ (3.1) for a solenoid (saddle) coil of similar dimensions, respectively [33]. For similar sample and rock dimensions, Eq. (C3) predicts the reduction (quoted in our Introduction) of ~245 in SNR, in going from 85 MHz (saddle-coil) to 2 MHz (solenoid).

### C.2. Saline flow-line noise

In the present case, however, the conductive saline solution in the rock and its flow loop back to the pumps added an extra noise term. We first verified that just placing the brine filled rock (i.e. a conducting sample) inside the coil *without* any connections to the flow loop had no effect on the noise. We also verified that the conductive sample did not significantly alter the $Q$ (~11) of the probe, since $Q$ alters the SNR ~ $Q^{1/2}$ [33]. However, once we connected the brine flow loop to the rock, there was clearly an extra noise term. The observed salinity dependence of SNR at 2 MHz is shown in Fig. 9 against the salinity (conductivity) of the flowing water in the rock, from deionized water up to 5 S m$^{-1}$ brine, with fits to Eq. (C8). One experimental set-up grounded the flowing saline circuit to the NMR spectrometer's common ground via the steel frame assembly (see Fig. 1). The other set-up had no such grounding, which leaves the flow loop floating. It is clear that grounding the flow line helps reduce the noise, and the overall

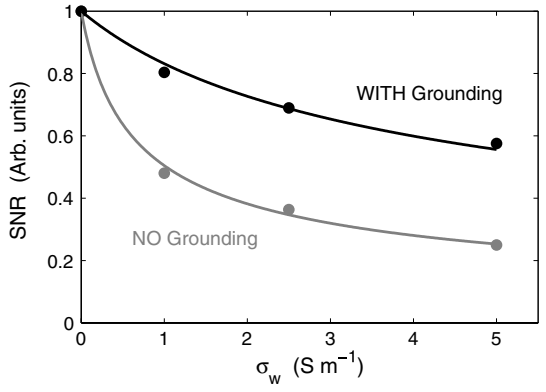


Fig. 9. Signal-to-noise ratio SNR (arbitrary units) vs. the conductivity $\sigma_w$/S m$^{-1}$ of the flowing water, from deionized water up to 5 S m$^{-1}$ brine solution. One experimental set-up grounded the flowing brine to the NMR spectrometer common ground, while the other did not. Lines are fits to the functional form of Eq. (C8).

penalty in using brine instead of deionized water is to signal average $n_{sc} \sim 4$ times more.

Defining the extra noise term from the saline flow-loop as $N_\sigma$, we deduce that the total noise is now

$$N \simeq \left(N_R^2 + N_\sigma^2\right)^{1/2}, \tag{C.4}$$

given that $N_R$ and $N_\sigma$ are independent and can thus add in quadrature. Using Eq. (C4) and taking $N_R \simeq 5\times10^{-8}$ V Eq. (C2), we find from Fig. 9 that $N_\sigma \simeq 6\ (18)\times10^{-8}$ V for the grounded (not grounded) arrangement, respectively, at high salinity (5 S m$^{-1}$). In other words the two sources $N_\sigma \gtrsim N_R$ are comparable at high salinity, and the total noise is enhanced when using a highly saline flow-loop.

By using a simple transformer picture we can model the effect of the conductive flow loop. We start with the basic transformer equation $N_\sigma = M\dot{I}$ [46] which relates the voltage $N_\sigma$ induced in the NMR coil (secondary coil) to the rate of change of current $\dot{I}$ in flow loop (primary coil), given their mutual inductance $M$. Taking the Fourier transform (and then magnitude) of the transformer equation then results in

$$N_\sigma = M\omega_0 I(\omega_0) \tag{C.5}$$

where $I(\omega_0)$ is the r.m.s. current at frequency $\omega_0$ in the flow line. $I(\omega_0)$ can be estimated by equating the power dissipation in the flow lines (left hand side) to the power spectra density of the noise in the atmosphere (right hand side) as such

$$\frac{\ell}{A\sigma_w} I(\omega_0)^2 = S\cdot P(\omega_0)\Delta v \tag{C.6}$$

where $\sigma_w$ is the flowing fluid conductivity (which depends on salinity and temperature), $\ell(A)$ is the length (cross-sectional area) of the flow line, $S$ is the area of the conducting flow loop, and $P(\omega_0)$ is the power spectral density of the noise in units of W Hz$^{-1}$ m$^{-2}$ [46]. In general $P(\omega_0)$ decreases with increasing frequency with a power law exponent $n$, also known as "$1/f^n$" noise, where typically $1 \leqslant n \leqslant 2$. We therefore assume $P(\omega_0) \simeq \alpha_n/\omega_0^n$ with constant $\alpha_n$. Equating Eqs. (C5) and (C6) we obtain the following expression for the flow line noise

$$N_\sigma \simeq \left(a_f \Delta v \sigma_w\right)^{1/2} \omega_0^{1-n/2} \tag{C.7}$$

where $a_f = M^2\alpha_n SA/\ell$. Combining Eqs. (C2), (C4) and (C7) results in the final expression

$$\mathrm{SNR} \simeq \frac{\phi V_s n_{sc}^{1/2}}{a g_0 (F\Delta v)^{1/2} T_s} \frac{\omega_0^2}{\left(\omega_0^{1/2} T_c + a'\omega_0^{2-n}\sigma_w\right)^{1/2}} \tag{C.8}$$

where we combine the constants $a' = a_f/a_c$ for better comparison with Eq. (C3). Fig. 9 shows the results of the fit to Eq. (C8), which is found to be consistent with the data. We note that for $n = 1$ and the same $a'$, Eq. (C8) predicts that the reduction in SNR due to a saline flow loop becomes more severe at higher frequency.

## References

[1] R. Akkurt, H.J. Vinegar, P.N. Tutunjian, A.J. Guillory, Transaction of SPWLA 36th Annual Logging Symposium paper N (1995).
[2] M.D. Hürlimann, L. Venkataramanan, C. Flaum, P. Speier, C. Karmonik, R. Freedman, N. Heaton, Transaction of SPWLA 43rd Annual Logging Symposium paper FFF (2002).
[3] K.J. Packer, J.J. Tessier, Mol. Phys. 87 (1996) 267.
[4] Y.E. Kutsovsky, L.E. Scriven, H.T. Davis, B.E. Hammer, Phys. Fluids 8 (1996) 863.
[5] A. Ding, D. Candela, Phys. Rev. E 54 (1996) 656.
[6] J.D. Seymour, P.T. Callaghan, J. Mag Res. Ser. A 122 (1996) 90.
[7] L. Lebon, L. Oger, J. Leblond, J.P. Hulin, N.S. Martys, L.M. Schwartz, Phys. Fluids 8 (1996) 293.
[8] L. Lebon, J. Leblond, J.P. Hulin, Phys. Fluids 9 (1997) 481.
[9] J.D. Seymour, P.T. Callaghan, AIChE J. 43 (1997) 2096.
[10] J.J. Tessier, K.J. Packer, Phys. Fluids 10 (1998) 75.
[11] B. Manz, P. Alexander, L.F. Gladden, Phys. Fluids 11 (1999) 259.
[12] U.M. Scheven, P.N. Sen, Phys. Rev. Lett. 89 (2002) 254501.
[13] U.M. Scheven, J.G. Seland, D.G. Cory, Phys. Rev. E 69 (2004) 021201.
[14] U.M. Scheven, D. Verganelakis, R. Harris, M.L. Johns, L.F. Gladden, Phys. Fluids 17 (2005) 117107.
[15] D.J. Holland, U.M. Scheven, A.P.J. Middelberg, L.F. Gladden, Phys. Fluids 18 (2006) 033102.
[16] A.J. Moulé, M.M. Spence, S.-I. Han, J.A. Seeley, K.L. Pierce, S. Saxena, A. Pines, Proc. Natl. Acad. Sci. USA 100 (2003) 9122.
[17] J.A. Seeley, S.-I. Han, A. Pines, J. Magn. Reson. 167 (2004) 282.
[18] J. Granwehr, E. Harel, S.-I. Han, S. Garcia, A. Pines, P.N. Sen, Y.-Q. Song, Phys. Rev. Lett. 95 (2005) 075503.
[19] W.E. Kenyon, P.I. Day, C. Straley, J.F. Willemsen, Soc. Petrol. Eng. Form. Eval. 3 (1988) 622, Erratum: Soc. Petrol. Eng. Form. Eval., 4 (1989) 8.
[20] K.J. Packer, Encyclopedia of NMR, in: D.M. Grant, R.K. Harris (Eds.), Diffusion and Flow in Fluids, Wiley, New York, 1996, p. 1615.
[21] P.N. Sen, Concepts Magn. Res. A 23A (2004) 1.
[22] G.I. Taylor, Proc. R. Soc. London 219 (1953) 186.
[23] G.I. Taylor, Proc. R. Soc. London 225 (1954) 473.
[24] P.-G. de Gennes, J. Fluid Mech. 136 (1983) 189.
[25] H.O. Pfannkuch, Rev. Inst. Fr. Pétrol. 18 (1963) 215.
[26] K.H. Coats, B.D. Smith, Soc. Petrol. Eng. J. 231 (1964) 73.
[27] D. Khandai, D. Hlushkou, A.G. Hoekstra, P.M.A. Sloot, H.V. As, U. Tallarek, Phys. Rev. Lett. 88 (2002) 2345011.
[28] M.D. Hürlimann, J. Magn. Reson. 131 (1998) 232.

[29] G. Leu, E.J. Fordham, M.D. Hürlimann, P. Frulla, Magn. Reson. Imaging 23 (2005) 305.
[30] E.O. Stejskal, J.E. Tanner, J. Chem. Phys. 42 (1965) 288.
[31] J.E. Tanner, J. Chem. Phys. 52 (1970) 2523.
[32] U.M. Scheven, J. Magn. Reson. 174 (2005) 338.
[33] D.I. Hoult, R.E. Richards, J. Magn. Reson. 24 (1976) 71.
[34] A.E. Scheidegger, The Physics of Flow Through Porous Media, Univ. Toronto Press, Toronto, 1974.
[35] S. Meiboom, D. Gill, Rev. Sci. Instrum. 29 (1958) 688.
[36] R.M. Cotts, M.J.R. Hoch, T. Sun, J.T. Marker, J. Magn. Reson. 83 (1989) 252.
[37] E.J. Fordham, S.J. Gibbs, L.D. Hall, Magn. Reson. Imaging 12 (1994) 279.
[38] M.D. Hürlimann, K.G. Helmer, L.L. Latour, C.H. Sotak, J. Magn. Reson. A 111 (1994) 169.
[39] P.Z. Sun, J.G. Seland, D.G. Cory, J. Magn. Reson. 161 (2003) 168.
[40] R. Duplay, P.N. Sen, Phys. Rev. E 70 (2004) 066309.
[41] U.M. Scheven, J.G. Seland, D.G. Cory, Magn. Reson. Imaging 23 (2005) 363.
[42] R.L. Kleinberg, S.A. Farooqui, M.A. Horsfield, J. Colloid Interface Sci. 158 (1993) 195.
[43] Y.-Q. Song, S. Ryu, P.N. Sen, Nature 406 (2000) 178.
[44] M.D. Hürlimann, L. Venkataramanan, J. Magn. Reson. 157 (2002) 31.
[45] C.P. Lindsey, G.D. Patterson, J. Chem. Phys. 73 (1980) 3348.
[46] J.D. Jackson, Classical Electrodynamics, John Wiley, London, 1975.